Control of the Oxygen and Cobalt Atoms Diffusion through Co Nanoparticles Differing by Their Crystalline Structure and Size

*Zhijie Yang, Nailiang Yang, Jianhui Yang, Johanna Bergström, and Marie-Paule Pileni**

The size-dependent Kirkendall effect is studied by using Co nanoparticles. The sizes of Co nanoparticles differing by their crystal structures called nanocrystallinity, namely amorphous, polycrystalline *fcc*, single crystalline *hcp*, and single crystalline ε phase, are modulated from 4 to 10 nm. The nanoparticles self-assembled in 2D superlattices and differing by their nanocrystallinities are subjected to oxygen at 200 °C for 10 min. With single-domain nanocrystals differing by their crystalline structure (ε and *hcp* phases), marked changes in the final structures are observed: upon increasing the nanocrystal size, the ε phase favors formation of a hollow structure whereas a transition from single-domain hollow to multidomain core/shell structures takes place with the *hcp* phase. With polycrystalline *fcc* Co nanocrystals, a transition from a hollow to a yolk/shell structure is observed, whereas with amorphous cobalt, solid CoO nanoparticles are produced at the smaller size and are converted to the core/shell structure at the larger one. These differences in size effect are attributed to the change in the control of the inward flow of oxygen atoms and the outward flow of Co atoms with the crystalline structure of cobalt nanoparticles. Such a diffusion process described here on the Kirkendall effect can be studied for other metal nanocrystals.

1. Introduction

Metallic nanomaterials and their oxides are considered as a kind of promising candidates for application in modern science and technology, especially, the porous solid materials have potential uses in ion exchange, molecular separation, catalysis, microelectronics, and energy storage, owing to their high surface area and internal void morphology.[1–5] Among them, cobalt and its oxides are considered to be ideal materials for magnetic fluids, spintronics, catalysis, and Li-ion batteries.[6–11] Interestingly, partially oxidized Co nanoparticles show a different magnetic phenomenon because of the magnetic exchange coupling between the ferromagnetic core and antiferromagnetic shell,[12–14] thus the study of the oxidation process is needed in order to precisely control the magnetic properties of the heterostructured nanoparticles. The nanoscale Kirkendall effect well explains the oxidation process and void formation based on the diffusivity differences through the interface, between the metal nanoparticles and their oxides. When the outward diffusion of metal cations is much faster than the inward diffusion of anions, vacancies will inward diffuse concomitantly. Several small vacancies will coalesce into a larger void, and then a hollow nanoparticle forms.[1,15,16] Also, the size distribution shows a clear effect on the physical properties.[17] A former study has found that besides the atomic diffusion, crystalline structure and other aspects are also related to the Kirkendall effect.[18–20] Our recent study presented that the 2D ordering and crystallinity can also affect the oxidation of cobalt.[19–21] Meanwhile, oxygen diffusion is different between 2D superlattices and isolated particles, and the resulting different oxidation processes.[19] The stability of Co was remarkably improved when the particles are self-assembled into a compact hexagonal network.[19] Meanwhile, various crystallinities also showed different oxidation results among all the 2D-ordered superlattices.[21]

Here, in this paper, we produce a series of cobalt nanoparticles with differing crystalline structures (ε, *hcp*, *fcc*, and amorphous) and sizes. The critical size-dependent morphology transition on the oxides based on Kirkendall effect is studied.

2. Results and Discussion

Co nanoparticles, self-assembled in a 2D hexagonal network, differing by their sizes and crystal structures are subjected to an oxidation process. A careful characterization is performed with each sample. As an example, we present here a typical characterization performed on Co nanoparticles having 8 nm as average diameter with a low size distribution and differing

Dr. Z. Yang, Dr. N. Yang, Dr. J. Yang, J. Bergström, Prof. M.-P. Pileni
Sorbonne Universités
UPMC Univ Paris 06, UMR 8233
MONARIS F-75005, Paris, France
E-mail: mppileni@orange.fr
Dr. Z. Yang, Dr. N. Yang, Dr. J. Yang, J. Bergström, Prof. M.-P. Pileni
CNRS, UMR 8233, MONARIS F-75005, Paris, France
Prof. M.-P. Pileni
CEA/IRAMIS, CEA Saclay 91191, Gif-sur-Yvette, France

DOI: 10.1002/adfm.201403617

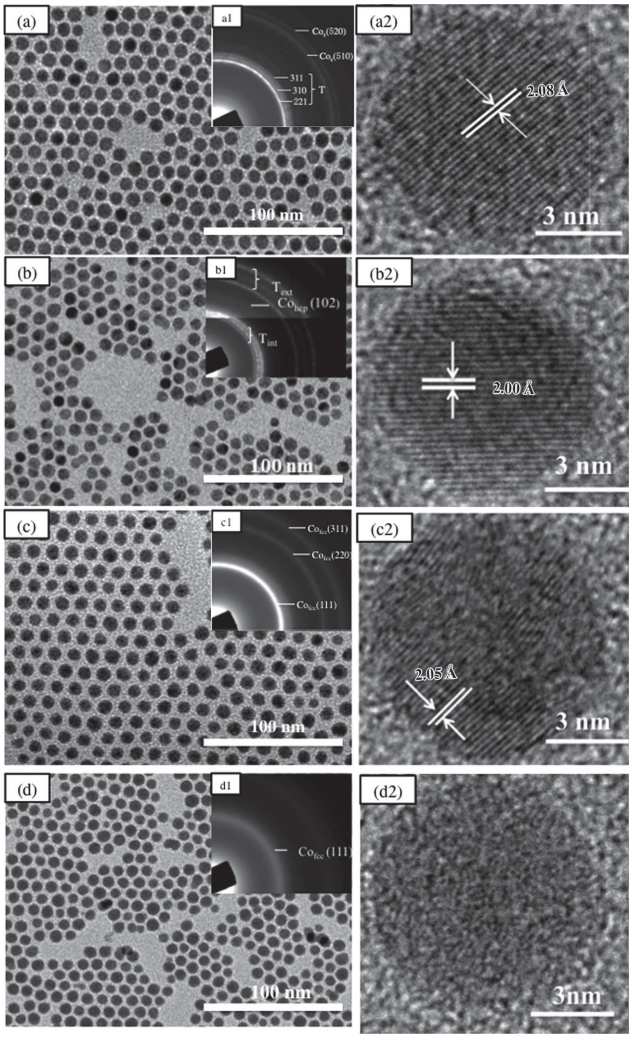

Figure 1. Structure characterization of 8 nm cobalt nanoparticles with different crystal forms. (a–d) refer to the cobalt with *ε*, *hcp*, *fcc*, and an amorphous phase, respectively and (a1, b1, c1, d1) represent the electron diffraction (ED) patterns of corresponding cobalt crystal phase. Tint and Text marked on the ED patterns in Figure (b1) refer to the internal triplet rings [(100), (101), (002)] and external triplet rings [(110), (103), (112)], respectively. The HRTEM images of cobalt polymorphism are shown in Figure (a2, b2, c2, d2). The $Co_{epsilon}$ and Co_{HCP} is single crystalline, while the Co_{FCC} is polycrystalline.[21–27]

by their nanocrystallinities (morphology characterizations of other products were exhibited in Supporting Information). Based on the TEM analysis of the nanoparticles before oxidation (**Figure 1**a–d), their crystalline structure is assigned from the selected area electron diffraction (SAED) rings (Figures a1–d1 in Figure 1) of the typical crystal facets of the nanoparticles. The high-resolution TEM (HRTEM) images showed the well-defined single-domain particles of $Co_{epsilon}$ and Co_{HCP}, and the multidomain Co_{FCC}.[21–27] The corresponding interplanar lattice fringes can also be attributed to the Co, respectively.

A similar study is performed after oxidizing the sample. It is found that Co nanoparticles evolve to CoO (oxide) materials. This is assigned through SAED and HRTEM measurements. A specific feature of the SAED pattern with a ring at 2.46 Å,

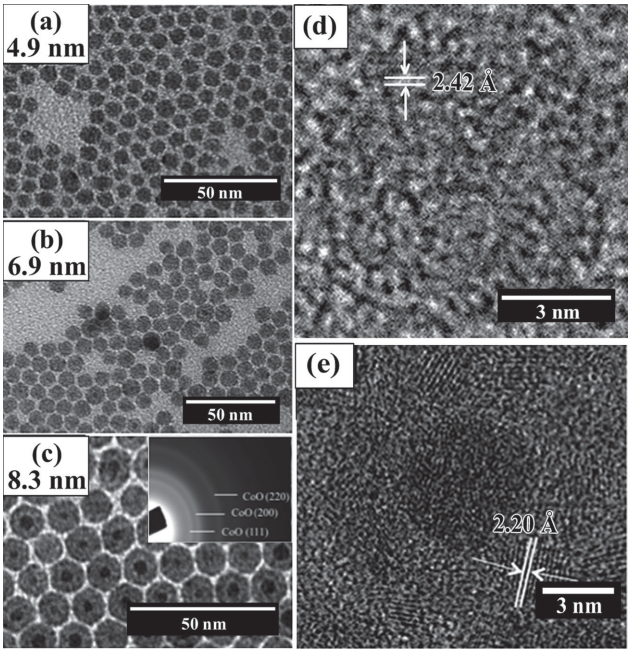

Figure 2. Morphology characterization of Co_A after oxidation. The solid spheres were obtained from a) 4.9 nm Co and the core/shell structure was obtained from c) 8.3 nm Co. 6.9 nm Co will form the mixture of solid and core/shell products (b). d) HRTEM of (a), indicating that only a faint crystal lattice was observed. e) HRTEM of (c), indicating that the CoO shell was formed.

indicative of the (111) lattice spacing is observed (see below). From HRTEM patterns, lattice fringes with interplanar spacings at 2.11 and 2.46 Å are seen that were indexed as (200) and (111) reflections of the cubic CoO lattice.

Let us first consider the amorphous cobalt nanoparticles (Co_A) differing by their sizes. Before the oxidation process, the average diameters and size distributions of Co_A nanoparticles are 4.9 nm, 6.9 nm, 8.3 nm, 9.8%, 8.7%, and 9.3%, respectively. After the oxidation they evolve to 6.8 nm, 8.1 nm, 10.6 nm, 7.9%, 8.3%, and 9.2%, respectively. **Figure 2** shows that for any nanoparticle size, solid nanoparticles are produced after oxidation. With 4.9 nm Co_A nanoparticles, the TEM image (Figure 2a) shows a high homogeneous contrast. The HRTEM image (Figure 2d) shows very weak crystal lattice fringes corresponding to CoO. On increasing Co_A nanoparticles size to 6.9 nm, most of the nanoparticles present a homogeneous contrast whereas some of them exhibit a core/shell structure (Figure 2b). Considering the Co nanoparticles are amorphous, in this case, the core/shell structures are induced by the larger sized Co nanoparticles due to the 10% size distribution. A further increase in the Co_A nanoparticle size to 8.1 nm reveals that the nanoparticles' contrasts are no longer homogeneous and exhibit a core/shell structure (Figure 2c) with a shell thickness around 3.5 nm. Note that the shell is composed of a polycrystalline CoO layer. Moreover, the nanoparticles appear to have a sixfold symmetry that is probably due to the 2D hexagonal ordering of the Co nanoparticles, providing a steric confinement during the oxidation inducing volume expansion. This transition from a solid to a core/shell structure is due to the fact that oxygen atoms are adsorbed on the oxide surface, and

electrons can transport rapidly through the oxide by tunneling to establish equilibrium diffusion between cobalt and adsorbed oxygen. The resulting electric field in the oxide layer facilitates the passage of cobalt ions across the oxide layer. However, after a certain thickness of oxide film formation, the ion transport becomes difficult to take place. Hence, without a stronger thermal driven force, the oxide layer would increase quite slowly and the core/shell structure is formed, which is confirmed by the Cabrera–Mott theory.[15,29]

Instead of Co_A nanoparticles, let us consider single-domain nanocrystals characterized with an ε crystalline structure, $Co_{epsilon}$. The average diameters and size distributions of $Co_{epsilon}$ nanocrystals before oxidation are: 5.5, 6.8, 8.7, 9.4 nm and 9.1%, 6.3%, 6.7%, 6.4% respectively. After oxidation they evolve to 6.7, 8.1, 10.1, 10.4 nm and 9.1%, 7.4%, 8.0%, 6.4%, respectively. For any $Co_{epsilon}$ nanocrystal size, hollow nanoparticles are produced with formation of multidomains of CoO crystalline phase (**Figure 3**a–d). Meanwhile, the shell thickness of the oxide and the cavity are enhanced with the increasing size of Co nanoparticles (**Table 1**, Figure S6 (Supporting Information)). Note that for 9.4 nm nanoparticles (Figure 3d), a few yolk/shell structures are observed. This clearly shows that Co atoms have a higher mobility than the oxygen ones, as a result of diffusing out of Co atoms and the accompanying vacancies were fluxed inward, concentrating at the interface of CoO as already explained by the nanoscale Kirkendall effect.[15,29]

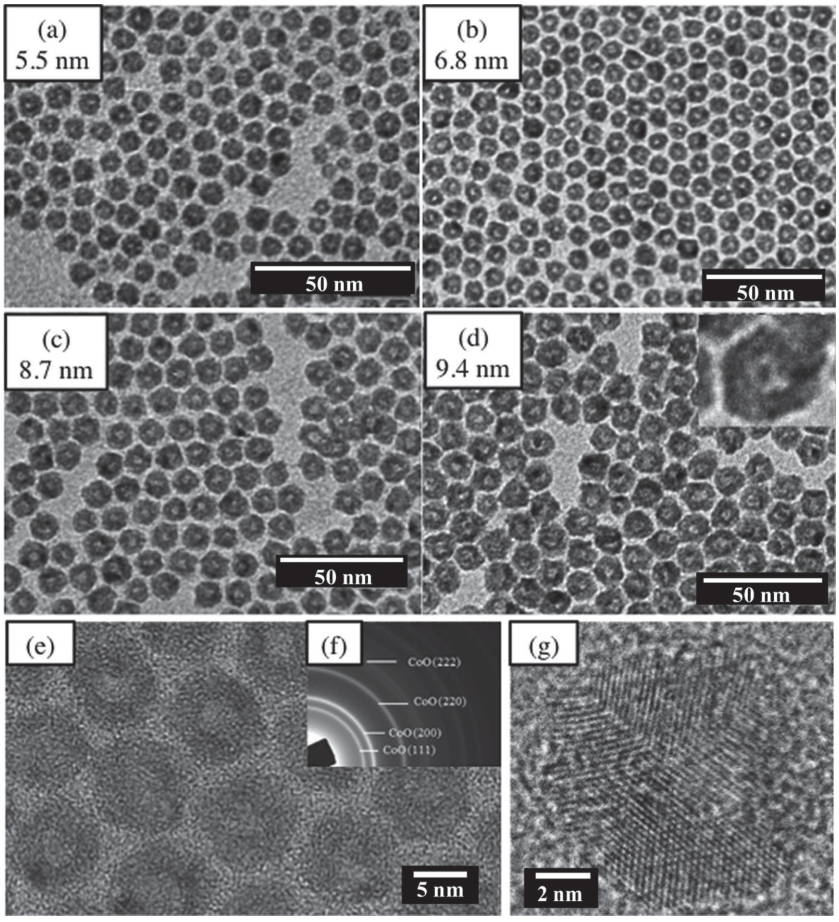

Figure 3. Morphology characterization of $Co_{epsilon}$ single-domain nanocrystals after oxidation. a–c) The hollow spheres were obtained from $Co_{epsilon}$ with different sizes. d) For 9.4 nm Co, quite a few yolk/shell structures were observed. e) HRTEM image and the ED pattern in (f) confirmed that the oxidative products are CoO. g) The HRTEM indicated the products were polycrystals.[21]

At this point, we can ask if the major differences observed between amorphous and epsilon phases of Co nanoparticles are related to the nanocrystallinity or not. To answer this question, let us consider the single-domain *hcp* Co nanocrystals (Co_{HCP} nanocrystals). The average diameters and size distributions of Co_{HCP} nanocrystals before oxidation are 4.7 nm, 6.8 nm, 8.4 nm, 13%, 9.7%, and 10%. After oxidation, they evolve to 6.1 nm, 8.0 nm, 9.4 nm, 12.4%, 10.4%, and 9.4%, respectively. The smaller Co_{HCP} nanocrystals (4.7 and 6.8 nm) produce CoO hollow nanocrystals (**Figure 4**a,b). The corresponding HRTEM images show the formation of single-domain CoO nanocrystals (Figure 4d) from 4.7 nm Co_{HCP} nanocrystals, whereas with 6.8 nm Co_{HCP} nanocrystals, the shell is a mixture of single- (Figure 4e) and multidomain (Figure 4f) hollow CoO nanoparticles. The cavity increases with increasing the Co_{HCP} nanocrystal size. However, it can be observed that the percentage of the cavity volume is slightly smaller for Co_{HCP} compared with $Co_{epsilon}$ nanocrystals (Table 1). Furthermore, there is the CoO shell crystalline transition from a single domain at a smaller size to a polycrystalline structure at a larger size, which is not observed with the $Co_{epsilon}$ nanocrystals. This clearly indicates a marked decrease in the relative Co and O atoms diffusion processes in Co_{HCP} nanocrystals compared with the $Co_{epsilon}$ ones. Such a lower outward diffusion of Co atoms is confirmed by increasing the Co_{HCP} nanocrystal size to 8.4 nm. Figure 4c shows formation of core/shell nanocrystals. The corresponding HRTEM image (Figure 4g) shows that the core remains a single-domain Co_{HCP} nanocrystal, whereas the shell is the CoO polycrystalline phase.

Both $Co_{epsilon}$ and Co_{HCP} are single-domain crystalline structures of nanocrystals, the major differences in the behavior are:

i) An increase in the volume of cavities with $Co_{epsilon}$ nanocrystals compared with the corresponding Co_{HCP} ones;
ii) The formation of core/shell (Co/CoO) nanocrystals with 8.4 nm Co_{HCP} nanocrystals whereas hollow nanoparticles with polycrystalline CoO are produced for $Co_{epsilon}$ with similar sizes (8.7 nm);
iii) The smaller Co_{HCP} nanocrystals size produces a single-domain CoO shell whereas CoO from $Co_{epsilon}$ ones has a polycrystalline structure.

These differences are related to the atomic capacities of the nanocrystals. The $Co_{epsilon}$ nanocrystals are characterized by a cubic crystalline structure less compact than the hexagonal

Table 1. Summary of size effect on different crystal phase.

Co_A	D_{before}[a] [nm]	4.9	6.9	8.3	
	D_{after}[b] [nm]	6.9	8.1	10.6	
	T_{shell}[c] [nm]	Solid	Mixture	Core/Shell	
$Co_{epsilon}$	D_{before} [nm]	5.5	6.8	8.7	9.4
	D_{after} [nm]	6.7	8.1	10.1	10.4
	T_{shell} [nm]	2.5 ± 0.3	2.9 ± 0.4	3.2 ± 0.5	3.2 ± 0.5
	D_{cavity}[d] [nm]	1.7	2.3	3.7	4.0
	Volume percentage of cavities [%]	1.6	2.3	4.9	5.7
Co_{HCP}	D_{before} [nm]	4.7	6.8	8.4	
	D_{after} [nm]	6.1	8.0	9.4	
	T_{shell} [nm]	2.5 ± 0.4	3.2 ± 0.5	Core/Shell	
	D_{cavity} [nm]	1.1	1.6		
	Volume percentage of cavities [%]	0.6	0.8		
Co_{FCC}	D_{before} [nm]	5.1	6.8	8.0	9.5
	D_{after} [nm]	6.3	8.3	9.7	11.9
	T_{shell} [nm]	2.4 ± 0.4	3.1 ± 0.5	3.2 ± 0.4	3.4 ± 0.4
	D_{cavity} [nm]	1.5	2.2	3.3	Yolk/Shell
	Volume percentage of cavities [%]	1.3	1.9	3.9	

[a] D_{before} is the diameter before oxidation; [b] D_{after} is the diameter after oxidation; [c] T_{shell} is the thickness of shell after oxidation. $T_{shell} = (D_{after} - D_{core})/2$, where D_{after} is the outer diameter of the nanoparticles determined by edge-to-edge distance for anisotropic particles; [d] D_{cavity} is the diameter of the cavity after oxidation.

structure of Co_{HCP} and consequently, the diffusions of Co atoms are increased and consequently that of O atoms slow down.

The differences in the data obtained between two single-domain Co nanocrystals in the same size range could be related to the different atoms' packing in single-domain nanocrystals (*hcp* and epsilon phase). Unfortunately, it is impossible to produce single-domain *fcc* nanocrystals having a packing model that is similar to *hcp* but different from epsilon. Here, we produce polycrystalline *fcc* nanocrystals (Co_{FCC} nanocrystals) with rather large single domains (**Figure 5**). The interplanar spacing distance observed from Figure 5 shows various HRTEM images with the (111) lattice planes of *fcc* Co nanocrystals differing by their sizes. In all the experimental conditions, polycrystalline structures characterized by average sizes and distributions of: 5.1 nm, 6.8 nm, 8.0 nm, 9.5 nm, 9.7%, 8.8%, 8.8%, and 7.4%, respectively are produced. At the end of the oxidation processes, the corresponding average sizes and size distribution are 6.3 nm, 8.3 nm, 9.7nm, 11.9 nm, 9.5%, 9.6%, 8.2%, and 7.6%, respectively.

After oxidation of 5.1 nm Co_{FCC} nanoparticles, hollow nanoparticles (**Figure 6**a and inset) are produced. From HRTEM images, the CoO shell is polycrystalline with a large domain (Figure 6b,c). The shell thickness is similar for Co_{FCC} and Co_{HCP} whereas the cavity is larger for Co_{FCC} (Table 1). With 9.5 nm Co_{FCC}, yolk/shell structures are produced (**Figure 7**a and inset). The shell is composed of several crystallized domains (Figure 7b). Figure 7c shows that the core remaining is a single-domain Co even though before treatment the Co_{FCC} nanocrystals are polycrystalline. Note that with all the nanoparticle studied when the core is present, it keeps the same crystalline structure as it before oxidation. With 6.5 nm Co_{FCC} nanoparticles, the data remains similar to those obtained with 5.1 nm with formation of hollow nanocrystals (Supporting Information). With 8 nm Co_{FCC} nanoparticles, an intermediate situation between 5.1 and 9.5 nm CoO nanoparticles is obtained with formation of both hollow and yolk/shell structures (Supporting Information).

Table 1 and Figure S6 (Supporting Information) show that the shell thickness of Co_{FCC} increases with the increasing of the nanoparticle diameter as well as the cavity. Furthermore, the size of the cavity compared with the initial size of the oxidized nanoparticles are slightly larger compared with Co_{HCP} nanoparticles and smaller than the $Co_{epsilon}$ ones. Because both *hcp* and *fcc* are compact structures, we would expect to produce similar cavity size with similar outward and inward diffusions of Co and O atoms and consequently the same relative cavity sizes for both crystalline structures. In fact, the values obtained with Co_{FCC} are in between those of Co_{HCP} and $Co_{epsilon}$ nanocrystals. This can be easily explained by the fact that Co_{FCC} nanoparticles are not single domain in structure, and the presence of defects inside crystalline lattices yields a faster O diffusion rate through Co lattices. Table 1 reveals that for the Co nanocrystals of any form of crystalline structure, a critical CoO shell thickness for the transition between hollow nanoparticles to either core/shell or yolk/shell structure exists. This critical shell thickness is up to 3.2 nm. Considered the larger nanoparticles, after the formation of initial oxide layers, the migration velocity of Co and O atoms was slowed down in its oxide, which suppressed the further oxidation, leaving a core at the center. This agrees with a previous report for Ni nanoparticles where nanocrystallinity was not taken into account.[30]

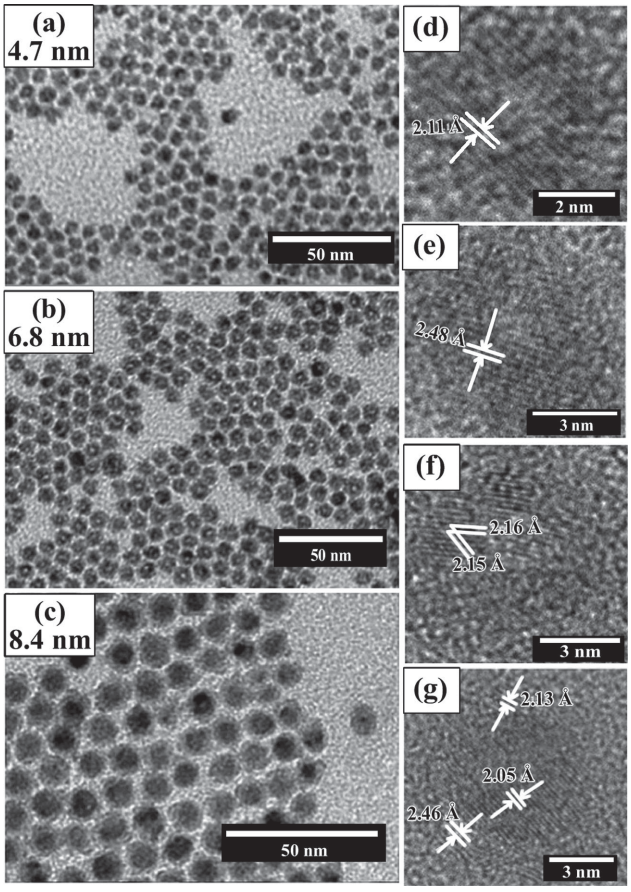

Figure 4. Morphology characterization of Co_{HCP} single-domain nanocrystal after oxidation. a,b) The hollow spheres were obtained from 4.7 and 6.8 nm Co_{HCP} nanocrystals. c) While for 8.4 nm Cobalt, well-defined core–shell structures were observed. d–g)The HRTEM images of the products. d) The single-domain nanocrystals were observed for the 4.7 nm cobalt nanoparticles after oxidation. While a mixture of e) single and f) poly crystals were observed for 6.8 nm nanoparticle after oxidation. g) For the core–shell product from 8.4 nm crystals, the shell was a polycrystal of CoO and the core was still cobalt.

The kinetic evolution during the oxidation process is of particular interest.[31,32] Mathematical models for the component diffusion, vacancy generation, and the accumulation of the vacancies into single void have been developed for metal–metal oxide systems incorporating growing boundaries.[33–35] A sophisticated model based on time-dependent diffusion kinetics and interdiffusion in a spherical object has been described as during the interdiffusion process between the diffusion couple with differing diffusivity, several small vacancies are generated, and with the supersaturation of vacancies, they are condensed into seveal large and eventually merged to a single void.[16] Here, at a given temperature, the above results reveal that the atomic packing inside the Co nanoparticles can determine the product after the oxidation process. The detailed analysis has been mentioned in the preceding parts of the paper, and here we want to clarify that the nanocrystallinity and crystal phase markedly affect the atoms diffusion in the particles. The amorphous nanoparticles can be considered as full of defets, which makes the atoms diffuse chaoticly and disorderedly, hence the

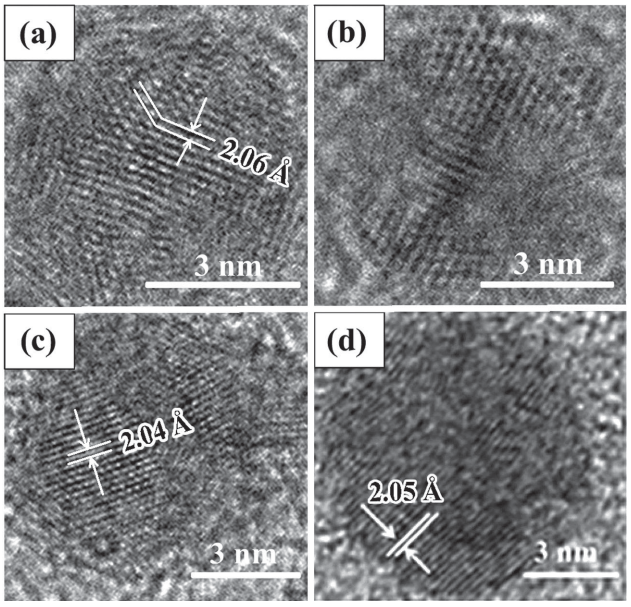

Figure 5. Various HRTEM images of a) 5, b) 6, c) 7, and d) 8 nm Co_{FCC} nanocrystals with large crystal domains.

oxidation process is very difficult and the core/shell structure forms. Contrarily, the perfect single crystals can make the atoms diffused along the lattices, which makes the oxidation easier. While for the polycrystals, besides the migration along the lattices, the long-range dislocation performs as the highway for atoms transporting, which let the diffusion fast. Herein, the

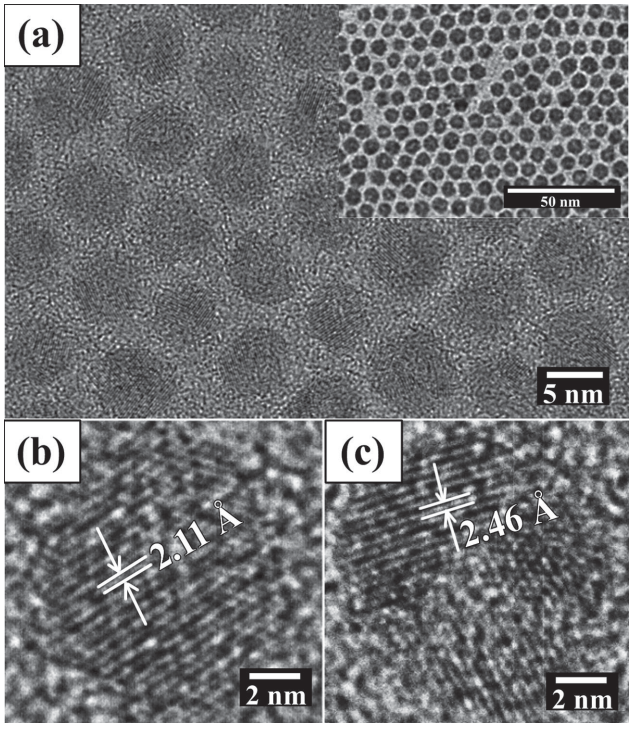

Figure 6. a) HRTEM image for the oxide from 5.1 nm Co_{FCC}. Inset long range TEM image. b,c) HRTEM images of oxidized nanocrystals with formation of polycrystalline oxide with large domain.

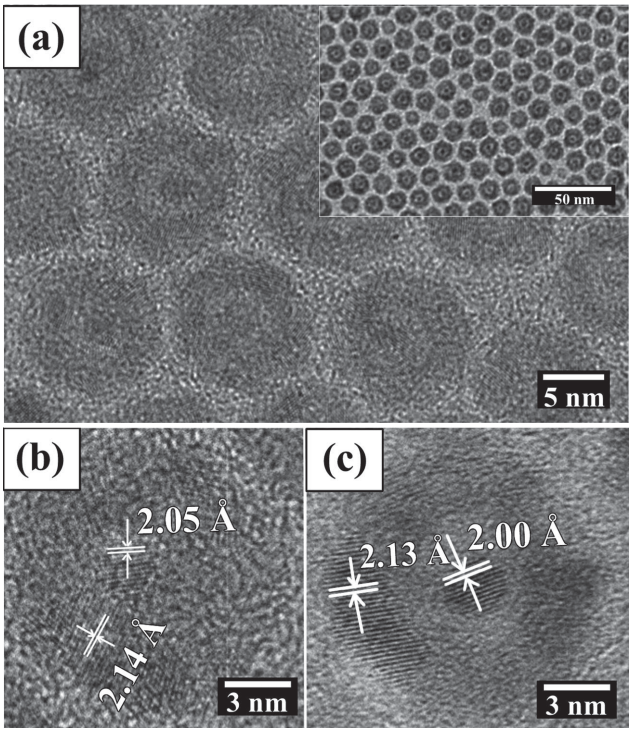

Figure 7. a) HRTEM image of yolk/shell nanocrystals produced from 9.5 nm Co_{FCC}. Inset long range TEM image. b,c) HRTEM images of the polycrystalline shell and single-domain *fcc* core.

diffusion route is affected by the crystallinity. Further analysis that comparing ε with *hcp* phase, although both single crystal, the different oxidation process was brought by the different atom packing. The closest packed *hcp* phase makes the atoms migration difficult, and bring the core/shell structure in the end. To further prove our understanding in the kinetic process, shorter period annealing treatment is introduced in the oxidation process (Supporting Information). Started from amorphous phase Co nanoparticles, although an initial oxide layer is formed after 1 min oxidation process (Figure S7a, Supporting Information), hollowing effect or a single void inside the nanoparticle cannot be observed after longer oxidation treatment. Although the interdiffusion between Co and O takes place in atomically disordered Co nanoparticles, and vacancies could be generated to compensate the materials flux, the condensation of the vacancies cannot be reached in the presence of plenty of crystal defects. On the contrary, in the case of the atomically orderd Co nanoparticles, a similar core/shell structure was obtained at the early stage (Figure S7b, Supporting Information), which can be defined as the mixture of Co and CoO, but the condensation of the vacancy can take place after reaching the supersaturation point. This experiment supported our kinetic analysis that the crystallinity quite affect the Kirkendall diffusion in the oxidation process.

3. Conclusion

In summary, different size-dependent oxygen diffusion processes are observed for Co nanoparticles with various crystal structures,

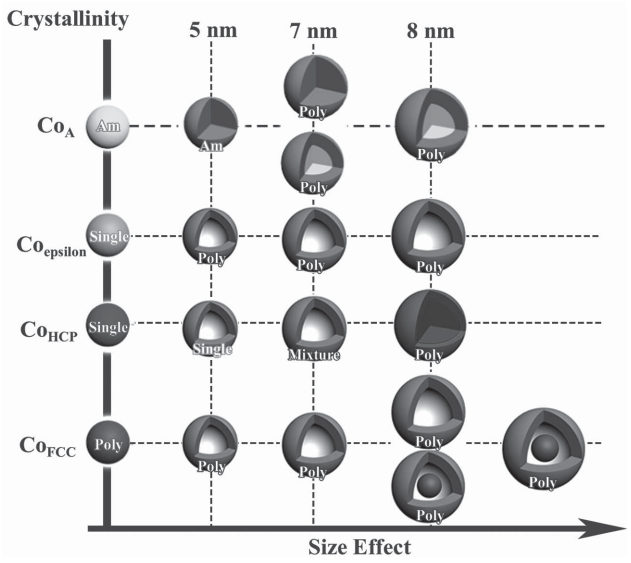

Scheme 1. Size dependence of Kirkendall effect with different crystallinities.

including epsilon and *hcp* single domain, *fcc* polycrystal, and amorphous cobalt. Based on the comparable size of different crystalline phases and the same experimental conditions, the result is given in **Scheme 1** and Table 1. For single-domain $Co_{epsilon}$ nanocrystals, no significant difference with the nanocrystal size is observed and consequently, polycrystalline CoO hollow nanoparticles are produced after oxidation. While for single-domain Co_{HCP} nanocrystals, a drastic size effect is observed: small-sized Co_{HCP} nanocrystals would result in the single-domain CoO hollow nanocrystals, whereas the large-sized Co_{HCP} nanocrystals lead to the formation of Co/CoO core/shell nanoparticles. By comparison between data obtained from compact crystalline structures (*hcp* and *fcc*), because of the presence of crystalline defects in Co_{FCC} (where there are no defects in *hcp* ones), polycrystalline CoO hollow or a yolk/shell structure can be produced with a faster diffusion of cobalt than oxygen atoms. For large nanocrystals, the thick oxide shell will also hamper further diffusion, forming a yolk/shell structure at the large size. Among all the Co nanoparticles investigated, only Co_A can form a solid nanoparticle without the observation of cavities. Here, we point out that the different size effect was related to i) the crystallinity of nanoparticles (amorphous, polycrystalline, or single domain); ii) the crystal phase of nanocrystals (epsilon or *hcp*); and iii) the critical thickness of the oxide layer. These data give a better understanding of the size effect on the nanoscale Kirkendall effect and can be studied for other metal materials, such as Ag, Ni, or Cu nanoparticles.[18,30,37]

4. Experimental Section

Synthesis of Co Nanoparticles Differing by their Nanocrystallinities: As described previously,[22,23] by adjusting the temperature in the hot injection method, single-domain nanocrystals with an ε phase as a crystalline structure ($Co_{epsilon}$) with various diameters are obtained. The average sizes and size distributions are 5.5, 6.8, 8.7 and 9.4 nm and 9.1%, 6.3%, 6.7%, 6.4%, respectively. By using reverse micelles as reported by our group,[24,25] amorphous cobalt nanoparticles (Co_A) are

produced with average diameters of 4.9, 6.9, and 8.3 nm, and the size distribution is 9.8%, 8.7%, 9.3%, respectively. As already described, a crystallographic transition from amorphous to *hcp* structure takes place by annealing Co_A nanoparticles at 250 °C under an inert atmosphere for 60 min and single-domain *hcp* nanocrystals are produced. Hence the Co_A nanoparticles are transformed to a single-domain *hcp* structure called Co_{HCP}. The annealing process does not significantly affect the nanocrystal diameter and its size distribution. The average diameters produced and size distributions are 4.7 nm, 6.8 nm, 8.4 nm and 13%, 9.7%, 10%, respectively. Note that the annealing treatment may cause damages to the coating agent, but it will not affect the subsequent oxidation progress as mentioned before.[19] The *fcc* cobalt nanocrystals (Co_{FCC}) are obtained by thermal decomposition of the cobalt carbonyl ($Co_2(CO)_8$) as previously described.[36] By adjusting the ligand concentration and decomposition temperature, the multidomain Co_{FCC} nanoparticles with 5.1, 6.8, 8.0, and 9.5 nm diameter are fabricated, and the size distribution is 9.7%, 8.8%, 8.8%, and 7.4%, respectively (Table 1). For any syntheses, the Co nanoparticles characterized by a low size distribution self-assemble in a compact hexagonal network (2D). The average diameters and size distributions were determined by measuring more than 500 particles from TEM images. The detailed synthetic procedures can be seen in Supporting Information.

Oxidation Process of Nanoparticles: During the oxidation process, all of the samples ($Co_{epsilon}$, Co_{HCP}, Co_{FCC}, and Co_A) are deposited on the TEM grid covered with a layer of amorphous carbon, and then simultaneously placed in a modified Schlenk line setup as reported (also shown in Supporting Information Scheme S1).[19,20] The heating setup was preadjusted to 200 °C. Then the annealing process was undertaken by subjecting the samples to pure oxygen. After 10 min, the heating setup was removed and the oxygen flow was replaced by an argon flow in order to stop the oxidation immediately. After cooling by an argon flow to room temperature, the samples are characterized by TEM.

Supporting Information

Supporting Information is available from the Wiley Online Library or from the author.

Acknowledgements

The research leading to these results has been supported by an Advanced Grant of the European Research Council under Grant 267129. Z.Y. thanks the China Scholarship Council for financial support. Z.Y. and N.Y. contributed equally to this work.

Received: October 16, 2014
Revised: November 25, 2014
Published online: December 18, 2014

[1] Y. Yin, R. M. Rioux, C. K. Erdonmez, S. Hughes, G. A. Somorjai, A. P. Alivisatos, *Science* **2004**, *304*, 711.
[2] S.-W. Kim, M. Kim, W. Y. Lee, T. Hyeon, *J. Am. Chem. Soc.* **2002**, *124*, 7642.
[3] X. W. Lou, L. A. Archer, Z. Yang, *Adv. Mater.* **2008**, *20*, 3987.
[4] J. Chen, F. Saeki, B. J. Wiley, H. Cang, M. J. Cobb, Z.-Y. Li, L. Au, H. Zhang, M. B. Kimmey, Li, Y. Xia, *Nano Lett.* **2005**, *5*, 473.
[5] K.-Y. Niu, J. Park, H. Zheng, A. P. Alivisatos, *Nano Lett.* **2013**, *13*, 5715.
[6] K. M. Shaju, F. Jiao, A. Debart, P. G. Bruce, *Phys. Chem. Chem. Phys.* **2007**, *9*, 1837.
[7] Y. Liang, Y. Li, H. Wang, J. Zhou, J. Wang, T. Regier, H. Dai, *Nat. Mater.* **2011**, *10*, 780.
[8] M. A. M. Gijs, F. Lacharme, U. Lehmann, *Chem. Rev.* **2009**, *110*, 1518.
[9] J. Wang, N. Yang, H. Tang, Z. Dong, Q. Jin, M. Yang, D. Kisailus, H. Zhao, Z. Tang, D. Wang, *Angew. Chem Int. Ed.* **2013**, *52*, 6417.
[10] C. T. Black, C. B. Murray, R. L. Sandstrom, S. Sun, *Science* **2000**, *290*, 1131.
[11] V. Puntes, K. Krishnan, A. P. Alivisatos, *Top. Catal.* **2002**, *19*, 145.
[12] C. Ge, X. Wan, E. Pellegrin, Z. Hu, S. Manuel Valvidares, A. Barla, W.-I. Liang, Y.-H. Chu, W. Zou, Y. Du, *Nanoscale* **2013**, *5*, 10236.
[13] S. E. Inderhees, J. A. Borchers, K. S. Green, M. S. Kim, K. Sun, G. L. Strycker, M. C. Aronson, *Phys. Rev. Lett.* **2008**, *101*, 117202.
[14] S. Guo, S. Zhang, L. Wu, S. Sun, *Angew. Chem Int. Ed.* **2012**, *51*, 11770.
[15] W. Wang, M. Dahl, Y. Yin, *Chem. Mater.* **2012**, *25*, 1179.
[16] Y. Yin, C. K. Erdonmez, A. Cabot, S. Hughes, A. P. Alivisatos, *Adv. Funct. Mater.* **2006**, *16*, 1389.
[17] B. Mehdaoui, A. Meffre, J. Carrey, S. Lachaize, L.-M. Lacroix, M. Gougeon, B. Chaudret, M. Respaud, *Adv. Funct. Mater.* **2011**, *21*, 4573.
[18] Y. Tang, M. Ouyang, *Nat. Mater.* **2007**, *6*, 754.
[19] Z. Yang, I. Lisiecki, M. Walls, M.-P. Pileni, *ACS Nano* **2013**, *7*, 1342.
[20] Z. Yang, M. Walls, I. Lisiecki, M.-P. Pileni, *Chem. Mater.* **2013**, *25*, 2372.
[21] Z. Yang, J. Yang, J. Bergstrom, K. Khazen, M.-P. Pileni, *Phys. Chem. Chem. Phys.* **2014**, *16*, 9791.
[22] D. P. Dinega, M. G. Bawendi, *Angew. Chem. Int. Ed.* **1999**, *38*, 1788.
[23] J. Yang, Kh. Khazen, M.-P. Pileni, *J. Phys. Cond. Mater.* **2014**, *26*, 295303.
[24] I. Lisiecki, S. Turner, S. Bals, M. P. Pileni, G. van Tendeloo, *Chem. Mater.* **2009**, *21*, 2335.
[25] Z. Yang, M. Cavalier, M. Walls, P. Bonville, I. Lisiecki, M.-P. Pileni, *J. Phys. Chem. C* **2012**, *116*, 15723.
[26] J. B. Tracy, D. N. Weiss, D. P. Dinega, M. G. Bawendi, *Phys. Rev. B* **2005**, *72*, 064404.
[27] I. Lisiecki, C. Salzemann, D. Parker, P.-A. Albouy, M.-P. Pileni, *J. Phys. Chem. C* **2007**, *111*, 12625.
[28] N. Cabrera, N. F. Mott, *Rep. Prog. Phys.* **1949**, *12*, 163.
[29] D.-H. Ha, L. M. Moreau, S. Honrao, R. G. Hennig, R. D. Robinson, *J. Phys. Chem. C* **2013**, *117*, 14303.
[30] J. G. Railsback, A. C. Johnston-Peck, J. Wang, J. B. Tracy, *ACS Nano* **2010**, *4*, 1913.
[31] H. J. Fan, U. Goesele, M. Zacharias, *Small* **2007**, *3*, 1660.
[32] H. J. Fan, M. Knez, R. Scholz, D. Hesse, K. Nielsch, M. Zacharias, U. Gösele, *Nano Lett.* **2007**, *7*, 993.
[33] A. M. Gusak, K. N. Tu, *Acta Mater.* **2009**, *57*, 3367.
[34] V. I. Levitas, H. Attariani, *J. Phys. Chem. C* **2012**, *116*, 54.
[35] R. A. Masumura, B. B. Rath, C. S. Pande, *Acta Mater.* **2002**, *50*, 4535.
[36] S. Peng, J. Xie, S. Sun, *J. Solid State Chem.* **2008**, *181*, 1560.
[37] L.-I Hung, C.-K. Tsung, W. Huang, P. Yang, *Adv. Mater.* **2010**, *22*, 1910.